Hindawi
Journal of Nanomaterials
Volume 2022, Article ID 5798824, 15 pages
https://doi.org/10.1155/2022/5798824

Research Article

Biogenic Synthesis of Magnetite Nanoparticles Using Leaf Extract of *Thymus schimperi* and Their Application for Monocomponent Removal of Chromium and Mercury Ions from Aqueous Solution

Sintayehu Tamenne Geneti,[1] Gemechis Asfaw Mekonnen,[1] H. C. Ananda Murthy,[1] Endale Tsegaye Mohammed,[2] C. R. Ravikumar,[3] Bedasa Abdisa Gonfa,[1] and Fedlu Kedir Sabir[1]

[1]*Department of Applied Chemistry, School of Applied Natural Science, Adama Science and Technology University, P.O. Box 1888, Adama, Ethiopia*
[2]*Department of Chemistry, College of Natural Science, Hawassa University, P.O. Box 05, Hawassa, Ethiopia*
[3]*Research Center, Department of Science, East West Institute of Technology, VTU, Bengaluru 560091, India*

Correspondence should be addressed to Bedasa Abdisa Gonfa; bedassa.abdissa@astu.edu.et
and Fedlu Kedir Sabir; fedluked130@gmail.com

Received 11 October 2021; Revised 2 March 2022; Accepted 2 April 2022; Published 15 April 2022

Academic Editor: Dong Kee Yi

Currently, plant templated synthesis of magnetite iron oxide nanoparticles (Fe_3O_4 NPs) was emerged for multifunctional purposes. In this study, the leaf extract of the plant *Thymus schimperi* was utilized to synthesize Fe_3O_4 NPs. The synthesized NPs were characterized by using technical tools such as X-ray diffraction (XRD) spectroscopy, Fourier transform infrared (FT-IR) spectroscopy, scanning electron microscopy-energy dispersive X-ray (SEM-EDX) analysis, and ultraviolet-visible (UV-Vis) spectroscopy, and thermal analysis (TGA-DTA). The XRD result corroborated the presence of desired phase formation having pure cubic face centered phase structure with average crystallite particle size ranging from 20 nm to 30 nm. SEM micrographs confirmed microstructural homogeneities and remarkably different morphology of Fe_3O_4 NPs. Mercury (II) and chromium (VI) removal efficiencies of Fe_3O_4 NPs were found to be 90% and 86% from aqueous solution at initial concentration of 20 mg/L, respectively. Various factors which affect the metal ion removal efficiency such as metal ion initial concentrations, pH, contact time, and adsorbent dosage were also studied. The optimum pH and contact time for chromium ion adsorption were pH 5 and 60 min and that of mercury were observed to be pH 7 and 90 min, respectively. The Langmuir isotherm was best fitted for sorption of Hg(II) ion, and the Freundlich isotherm was best fitted with sorption of Cr(VI) ion onto the surface of Fe_3O_4 NPs. The mechanism of adsorption of both Hg(II) and Cr(VI) ions was obeyed pseudo 2nd order kinetics. The recorded percent removal efficiencies revealed that these Fe_3O_4 NPs synthesized through *leaf extract of the plant called Thymus schimperi* have demonstrated excellent potentiality in the remediation of heavy metal ions. The synthesized Fe_3O_4 NPs were regenerated (reused) for adsorptive removal of Hg(II) and Cr(VI) for five consecutive cycles without significant loss of removal efficiency. Fe_3O_4 NPs were reused with only 4.17% loss of removal efficiency against Hg(II) and only 3% loss of removal efficiency against Cr(VI) metal ions.

1. Introduction

Pollution of water bodies due to some toxic heavy metal ions is increasing day by day because of increased environmental population and industrialization. Due to their hazardousness, non-biodegradability, and their long-time tenacity in nature, removal of these heavy metals from water bodies is very important [1] Different types of techniques currently used in the removal of heavy metals from wastewater are ion exchange flotation, membrane separation, adsorption, precipitation, biosorption, and electrochemical treatment processes [2–5]. In current days, most widely employed approach for the removal of heavy metal ions from water is adsorption process. Various types of adsorbent materials have got application in the removal of heavy metals, including activated carbon [2], silica gel supported materials [6], nanocellulose materials [7, 8], and metal oxides [9]. Among these mentioned adsorbent materials, magnetite nanomaterials (Fe_3O_4) NPs have distinguished themselves by their unique properties, such as larger surface area to volume ratio, magnetic nature, diminished consumption of chemicals, and has no contribution for secondary pollutants [9]. For the removal of heavy metal ions from contaminated water, magnetic separation has been combined with adsorption so as to enhance the decontamination process [10].

The interest in Fe_3O_4 NPs for heavy metal ions remediation has been increasing due to their enhanced reactivity as a result of very high surface area to volume ratio [11]. Fe_3O_4 NPs have gained special attention in water purification to remove cationic pollutants like heavy metals and dyes which could be attributed to their high separation efficiency, superior magnetic properties, simple manipulation process, placid operation conditions, and easy functionalization methods [12–14].

Synthesis of metal and metal oxide nanoparticles (NPs) using the extracts from different parts (mostly leaf) of the plant is the most effective, economical, and eco-friendly method. Plant extract mediated synthesis has recently gained significance due to its simplicity. The processes adopted for synthesizing metallic and metal oxide NPs by the application of plant extracts were explored to be easily scalable and more economical compared to the other methods which depend completely on the microbes and whole plants [15].

The two prominent toxic and carcinogenic metal ions, Hg(II) and Cr(VI), are normally found in various wastewaters from many industries including plating, mining, battery, and tanneries. Their accumulation in living organisms resulted in varieties of disorders and diseases [16]. Reports have shown that the concentration of Cr(VI) and Hg(II) ions in wastewater in Africa is above the WHO's permissible limit [17, 18]. Concentration of Cr(VI) in industrial wastewater is estimated in the range of 0.1 to 200 mg/L and recommended safe limit of Cr(VI) in drinking water is 0.05 mg/L [18, 19], and permissible concentration of Hg(II) in wastewater is 0.05gm/L [18, 19] and that of recommended safe limit in drinking water is 0.001gm/L [20, 21].

The recent surveys conducted by the U. S. Environment Protection Agency (EPA) on national water quality indicated that more than one-third of the lakes and about half of the rivers across the nation are getting polluted by the noxious discharges such as Hg(II) and chromium (VI) from industrial facilities [22].

Since mercury (II) and chromium (VI) pollution has been a significant challenge in the world; the researchers in the area are striving a lot to alleviate this problem. Towards this contribution, the present work was aimed to synthesize Fe_3O_4 NPs using leaf extract of the plant *Thymus schimperi*, and apply it for the remediation of Hg(II) and Cr(VI) ions from wastewater.

The plant *Thymus schimperi*, is a grass-like indigenous plant (Figure 1s in supplementary section) in Ethiopia and commonly known by its local name as "*Tosign*" [23], is used as reducing agent and capping agent in synthesis of Fe_3O_4 NPs in this work.

In this study, *Thymus schimperi* leave extract templated synthesis of Fe_3O_4 NPs was done by one reaction pot. The synthesized Fe_3O_4 NPs used as adsorbent materials for removal of Hg(II) and Cr(VI) ions from wastewater. The optimization of parameters such as pH, contact time and initial concentration of aqueous solutions, and adsorbent doses was performed against a set of batch adsorption of Hg(II) and Cr(VI) ions from wastewater. The kinetics of adsorption and isotherm models was evaluated to propose mechanism of adsorption.

2. Experimental Methods

2.1. Chemicals and Reagents. The chemicals (analytical grade) and reagents used in this work were ferric chloride hexahydrate ($FeCl_3.6H_2O$, Blulux Ltd, India), ferrous chloride tetrahydrate ($FeCl_2.4H_2O$, Atico, India), potassium dichromate ($K_2Cr_2O_7$, Blulux Ltd, India), mercury (II) chloride ($HgCl_2$. Blulux Ltd, India), sodium hydroxide (NaOH), ethanol (99.9%), HCl, H_2SO_4, $KMnO_4$, diphenylcarbazide (DPC) (Ranchem Industry and Trading, India), and distilled water.

2.2. Collection of Plant Leaves. Fresh, matured, and disease-free leaves of the plant, *Thymus schimperi*, were collected from Chilalo Mountain, East Arsi Zone, Oromia, Ethiopia, after conducting prior field surveys. The collected leaves of *Thymus schimperi* were used to make the aqueous extracts.

2.3. Preparation of Thymus schimperi Leaf Extract. The plant leaves were washed by using domestic water and then rinsed with distilled water many times. The wet leaves were allowed to air dry under shade at room temperature. The dried plant leaves were then stored for further use.

A 10 gm of powder of the plant leaves was boiled with 200 mL of distilled water under stirring at 80°C for about one hour until the color of the aqueous solution changes to light brown. The aqueous extract of the sample was cooled and filtered first with ordinary filter paper and then using Whatman filter paper. Then, the filtrate was stored in a refrigerator at 4°C for further experiments [24–26]. Figure 1 shows the flow chart of extraction of active compounds from powders of leaves of *Thymus schimperi* in distilled water.

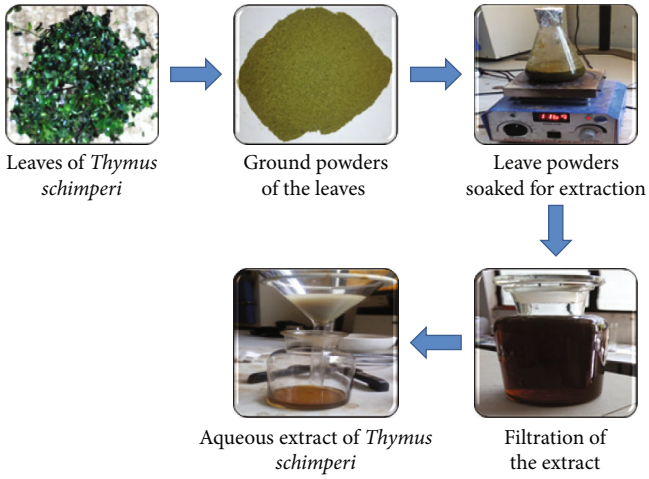

FIGURE 1: Flow chart of the extraction of active compounds from the powders of leaves of *Thymus schimperi* in distilled water.

2.4. Preparation of Precursor Salt Solution. Ferric chloride ($FeCl_3.6H_2O$) and ferrous chloride ($FeCl_2.4H_2O$) salt solutions were used in the synthesis of Fe_3O_4 NPs [27] using aqueous extract of *Thymus schimperi*. Ferric/ferrous salt precursor solutions were prepared by mixing and dissolving 13.6 gm of $FeCl_3.6H_2O$ and 5 gm of $FeCl_2.4H_2O$ salts in 500 mL of distilled water in 1000 mL volumetric flask. The mixture was stirred at room temperature for about 15 minutes and then stored for further use. Then, three different samples were prepared by taking different volume ratios of precursor salts solution with *Thymus schimperi* leaf extract.

2.5. Biogenic Synthesis of Fe_3O_4 NPs. In a typical experiment, the extract was added to ferric/ferrous chloride precursor solution in three different volume ratios. 50 mL of the extract was added to 100 mL of the precursor solution with 2 M NaOH for NPs (S12) preparation in one 250 mL conical flask, and then the solution mixture was labelled as (1 : 2). The second solution mixture (S11) was prepared by the addition of 100 mL of the extract to 100 mL of the precursor solution (1 : 1) with 2 M NaOH for NPs (S11) preparation in the second 250 mL conical flask. In the same way, the third solution mixture (S21) was prepared by adding 100 mL of the extract to 50 mL of the precursor solution (2 : 1) with 2 M NaOH. All the solutions were stirred continuously at 60°C for 1 hour to get a black precipitate (Figure 2). The precipitates were filtered using Whatman filter paper No 1 and washed repeatedly using distilled water and ethanol to remove impurities. Finally, the precipitate was dried in an oven at 60°C for 1 hour and ground to get fine powder. The black powder obtained was later calcined at 700°C for 1 hour [28].

2.6. Characterization Techniques. Thermal analysis was conducted using DTA-TGA instrument (DTG-60H, Shimadzu Co., South Korea) in order to decide the calcination temperature and to study thermal stability of the synthesized Fe_3O_4 NPs. A small amount of the powder was taken and the crystal structure of the Fe_3O_4 NPs was studied by using XRD-7000 X-Ray diffractometer, Shimadzu Co., Japan.

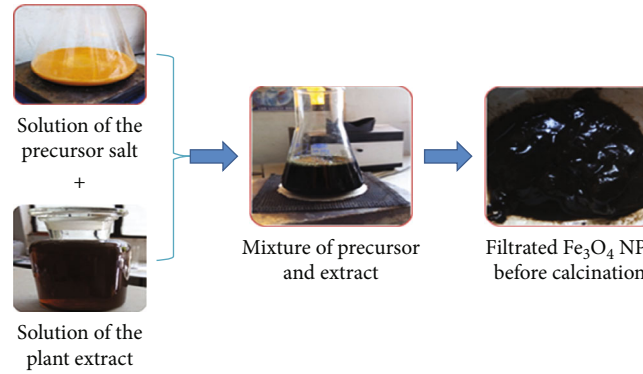

FIGURE 2: The schematic diagram of synthetic procedure for Fe_3O_4 NPs.

The FT-IR spectra of the synthesized Fe_3O_4 NPs were recorded using the instrument, Perkin Elmer65, PerkinElmer, Inc., Waltham, USA [29]. SEM-EDX (Carl Zeiss Model: Neon-40, FESEM/FIB, SMT, AG, Germany) analysis was also conducted to know the external morphology and chemical composition of the sample [30]. UV-Vis-diffuse reflectance spectrophotometer (Elico SL-150) was employed to measure the band gap energy of Fe_3O_4 NPs using Tauc equation (1), [31].

$$(\alpha h\upsilon)^{1/n} = A\left(h\upsilon - E_g\right), \tag{1}$$

where

α = absorption coefficient constant
$h\upsilon$ = photon energy
E_g = energy gap
n = ½ for allowed direct transition (Fe_3O_4 NPs)
n = 2 for allowed indirect transition

2.7. Preparation of Chromium (VI) and Mercury (II) Solutions. The stock solution of Cr(VI) was prepared by dissolving 2.826 g of $K_2Cr_2O_7$ in 1 L of distilled water. Similarly, 1.354 g of $HgCl_2$ was taken in 1 L of distilled water to get stock solution of Hg(II). The stock solutions were further subjected to dilution to obtain the desired concentration of standard solutions for absorbance measurement. 1, 5-diphenylcarbazide was used for spectrophotometric determination of Cr(VI). Potassium permanganate ($KMnO_4$) solution was prepared for color development of the mercury ion solution after adsorption. Full color development for these two solutions was formed and after 10 min, 4 mL of these solutions was used in an absorbance measurement cell (cuvette) and the concentrations were measured spectroscopically at 540 nm for chromium solution [32] and at 253.7 nm for mercury solution in UV spectrophotometer [33, 34].

2.8. Batch Adsorption Study. Batch adsorption studies were conducted to evaluate the efficiency of Fe_3O_4 NPs for the remediation of chromium (VI) and mercury (II) ions from the aqueous solutions. All the measurements were

performed in triplicates and the average values were reported. All the studies were executed at a temperature of 25°C (±0.5). The required pH of the solution was obtained by adding appropriate amounts of a mixture that contains solutions of 0.1 M NaOH and 0.1 M HCl. A calculated amount of the adsorbent was added to the sample with continuous agitation to attain adsorption equilibrium. The extent of removal of chromium and mercury ions was investigated separately by changing adsorption dose (100 mg, 300 mg, 500 mg, and 700 mg), contact time (30 min, 60 min, 90 min, and 120 min), initial concentration (20 mg/L, 40 mg/L, 60 mg/L, and 80 mg/L), and pH of the solution (3, 5, 7, 9, and 11). After adsorption, the separation of the adsorbent was achieved by filtration and the initial and final metal concentrations were deduced. The equilibrium adsorption capacity (Q_e) was calculated according to equation (2)

$$Q_e = \left(\frac{Co - Ce}{M}\right) V, \tag{2}$$

where

Q_e = equilibrium adsorption capacity (mg/g)

Co = initial liquid phase solute concentration (mg/L)

Ce = equilibrium liquid phase solute concentration (mg/L)

V = liquid phase volume (L)

M = amount of adsorbent (g)

In the same way, the present removal efficiency (%) of Fe_3O_4 NPs for chromium (VII) and mercury (II) heavy metals was deduced using the equation (3)

$$\text{Removal efficiency (\%)} = \frac{Co - Ce}{Co} \text{ x } 100, \tag{3}$$

where Co and Ce are the initial and equilibrium concentration after treatment with adsorbent. Optimum period of time to achieve maximum percent removal was determined.

2.9. Sorption Kinetics and Isotherm Studies

2.9.1. Sorption Kinetics Studies. The kinetics parameters associated with the adsorption process were determined for contact time varying between 1 and 120 min by monitoring the removal percentage for the Cr(VI) and Hg(II) ions.

2.9.2. Pseudo-First-Order Model. Pseudo-first-order rate model based on adsorption capacity of adsorbent is generally expressed as:

$$\log (Q_e - Q_t) = \log Q_e - k_1 t, \tag{4}$$

where Q_e and Q_t are the amounts (mg/g) of Cr(VI) and Hg(II) adsorbed at equilibrium and at time given (t), respectively.

Plot of log $(Q_e - Q_t)$ versus t gives a straight line for the 1st order adsorption kinetics through which rate constant k_1 is determined (Figure 2s in supplementary section).

2.9.3. Pseudo-Second-Order Model. The following equation describes the pseudo-second-order model in the linear form,

$$\frac{t}{q_t} = \frac{1}{k_2 q_e^2} + \frac{1}{q_e} t, \tag{5}$$

where

k_2 = adsorption rate constant (g/mg-min)

k_2 and q_e are found from the intercept and slop of t/q_t versus t linear plot such that q_e =1/slope and k_2 = slope^2/intercept

2.9.4. Sorption Isotherm Studies. The interaction between the solute particles and the adsorbent is provided by the adsorption isotherm. The Langmuir and Freundlich models are usually applied to explore equilibrium adsorption isotherms.

2.9.5. Langmuir Isotherm. The Langmuir isotherm (assumes monolayer adsorption) is represented by,

$$\frac{C_e}{q_e} = \frac{K_L C_e}{Q_o} + \frac{1}{Q_o}, \tag{6}$$

where q_e (mg/g) and C_e (mg/L) are the amount of adsorbed chromium or mercury per unit mass of sorbent and unadsorbed chromium or mercury concentration in solution at equilibrium, respectively. Q_o is the maximum adsorption at monolayer (mg g^{-1}) on the surface bound at high C_e, and K_L is a constant related to the affinity of the binding sites (L/mg).

The Langmuir constants Q_o and K_L were determined from the intercept and slope of the linear plot of (C_e/q_e) against the equilibrium concentration (C_e).

2.9.6. Freundlich Isotherm. Freundlich isotherm (an empirical equation) is usually employed to describe heterogeneous systems.

The Freundlich equation is expressed as:

$$q_e = K_f C_e^{1/n} \tag{7}$$

where K_f and n are Freundlich constants with K_f (mg/g (L/mg) $^{1/n}$) is the adsorption capacity of the sorbent and n giving an indication of how favorable the adsorption process. The magnitude of the exponent, $1/n$, gives an indication of the favorability of adsorption. Values of $n > 1$ represent favorable adsorption condition.

To determine the constants K_f and n, the linear form of the equation may be used to produce a graph of ln (q_e) against ln (C_e).

$$\ln q_e = \ln K_f + \left(\frac{1}{n}\right) \ln C_e. \tag{8}$$

Values of K_f and n are calculated from the intercept and slope of the plot (Figure 3s in supplementary section), respectively. If $n = 1$, then the partition between the two phases is independent of the concentration. If value of $1/n$

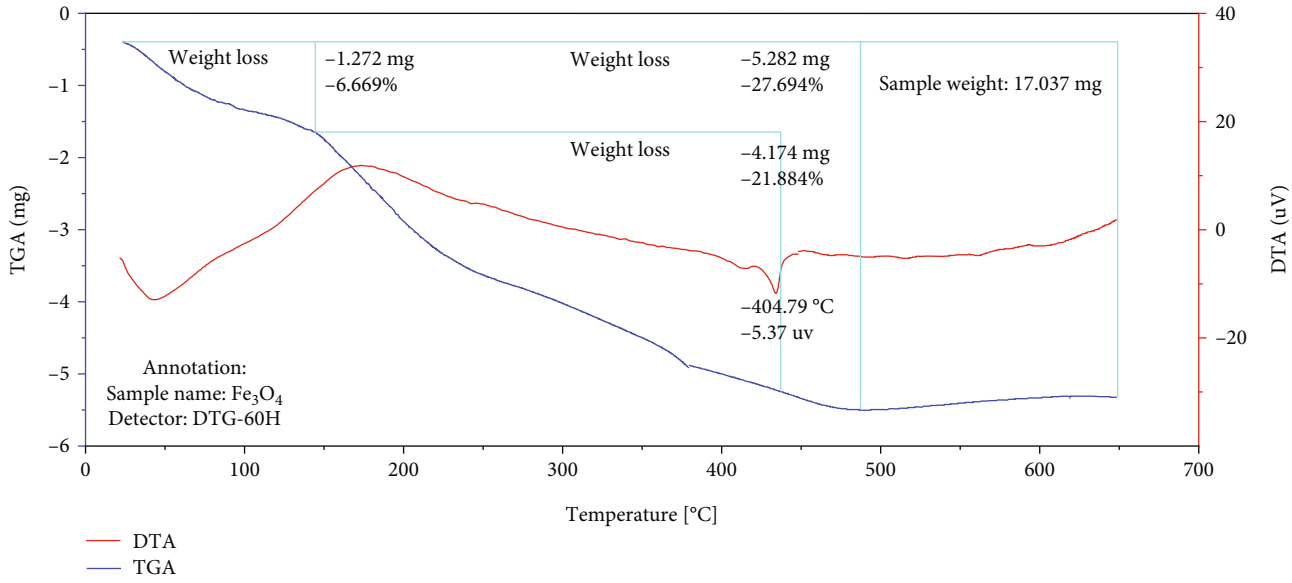

Figure 3: The TGA-DTA plots of uncalcined Fe_3O_4 NPs.

is below one, it indicates a normal adsorption. On the other hand, $1/n$ being above one indicates cooperative adsorption [20, 35].

3. Results and Discussion

3.1. TGA-DTA Analysis. The thermal analysis of the synthesized Fe_3O_4 NPs was conducted using TGA-DTA instrument. Figure 3 depicts TGA-DTA curves for the uncalcined sample of Fe_3O_4 NPs, two peaks in DTA curve (one endothermic peak at 160°C and one exothermic peak at 400°C), indicating two-step decomposition and weight removal of initial sample. The endothermic peak observed between 80 and 200°C can be attributed to the loss of water and low molecular weight phytochemicals of *Thymus schimperi* adhered to the NPs, the exothermic peak of DTA curve at 404.29°C; and 49.57% weight loss between 350°C and 450°C in TGA curve is possibly due to vaporization of carbonized residues present over the surface of the biogenic Fe_3O_4 NPs. As it can be observed in Figure 3, after temperature of 450°C, TGA curve became almost constant. The temperature beyond which the weight loss is constant is used as the calcination temperature of the synthesized Fe_3O_4 nanoparticles [36]. The temperature above which the weight loss of sample remained constant is taken as a calcination temperature. Calcination was performed at 450°C to remove unwanted remnants of the plant extract, and improve the purity of iron oxide NPs.

3.2. XRD Analysis. Figures 4(a)–4(c) depicts the XRD patterns of Fe_3O_4 NPs. As indicated in Figure 4, the XRD peaks of Fe_3O_4 NPs were observed at 2θ values, 30.15, 31.58, 35.49, 43.12, 45.26, 53.73, 57.11, 62.65° for S12; 30.06, 31.67, 35.42, 43.06, 45.38, 53.37, 56.42, 62.55° for S11; and at 30.06, 31.56, 35.41, 43.15, 45.25, 53.38, 56.83, 62.56° for S21. All the diffraction peaks observed are in compliance with the standard pattern for JCPDS Card No.79-0417 for Fe_3O_4 NPs [37]. The Miller indices, (220), (200), (311), (400), (220), (422), (511) and (440), observed for Fe_3O_4 NPs correspond to cubic spinel structure [38].

The average crystallite sizes of Fe_3O_4 NPs calculated using Debye-Scherer equation [37] are 20.26 nm, 29.12 nm, and 26.88 nm for S12, S11, and S21 samples, respectively.

The diffraction pattern of Fe_3O_4 NPs presented in Figure 4 (S11) was studied and the sharp intense peak obtained at 2θ values of 30.06, 31.67, 35.42, 43.06, 45.38, 53.37, 56.42, 62.55° corresponds to the lattice plane (220), (200), (311), (400), (220), (422), (511), and (440), respectively. All the diffraction peaks were well indexed to the hexagonal phase and crystallographic planes proving the structure of Fe_3O_4 NPs synthesized to be cubic structure [38].

3.3. FT-IR Analysis. FT-IR spectrum of the calcined green synthesized Fe_3O_4 NPs, as depicted in Figure 5(a), presents the strong absorption bands at 3440, 1622, 1425, 875, and 570 cm^{-1} while Figure 5(b) shows the absorption bands of uncalcined Fe_3O_4 NPs which were observed at 3420, 2959, 1623, 1456, 1377, 1064, and 600 cm^{-1}.

In the spectrum of the calcined Fe_3O_4 NPs, the wide absorption around 3440 cm^{-1} is caused by the presence of an O-H stretching vibrations from the absorbed water present over the surface of the NPs. The absorption peaks at 1622 cm^{-1} were attributed to the N-H bending of amide compound. 1425 cm^{-1} corresponded to the -CH_2 bending vibrations of the compound. Significant new peak was found at 875 cm^{-1} which corresponds to C-H bending. The presence of band at 570 cm^{-1} corroborates Fe-O stretching of Fe_3O_4 nanoparticles, as reported earlier [39].

Figure 5(b) depicts the FT-IR spectrum of uncalcined Fe_3O_4 NPs. The presence of strong and broad absorption band at 3420 cm^{-1} is caused by the presence of an O-H stretching vibrations of phytochemicals such as *Thymol* and Carvacrol [40] and was also due to absorbed water by

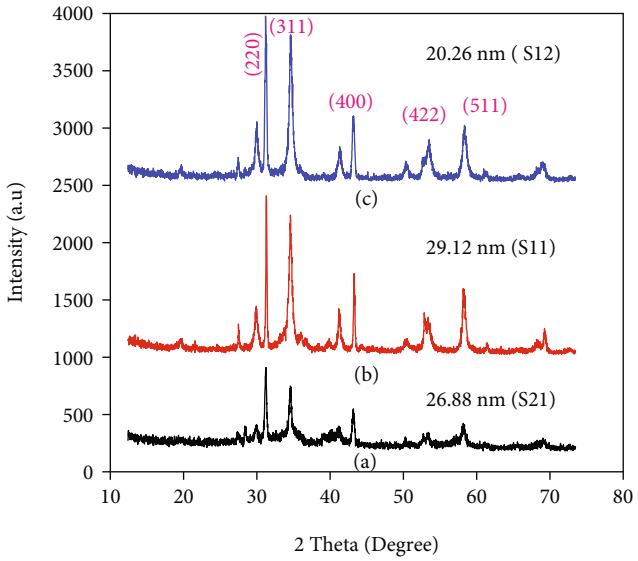

FIGURE 4: XRD pattern of synthesized Fe_3O_4 NPs in three different ratios of plant extract to precursor salt (a) S21 (2 : 1), (b) S11 (1: 1), and (c) S12 (1 : 2).

the sample. The presence of bands at 2959 cm^{-1} and 1456 cm^{-1} can be attributed to the -CH_2 stretching vibrations of the functional group [29]. The absorption band at 1623 cm^{-1} corresponds to the N-H bending vibrations of the compound and 1377 cm^{-1} to bending functional group of the O-H. The bands at 1051 cm^{-1} revealed the vibration of C-N bond and 600 cm^{-1} indicates C-O stretching band corresponding to the C-O-SO_3 group [41]. FT-IR absorption bands at 2340 cm^{-1} correspond to physisorbed CO_2 to surface of Fe_3O_4 NPs from the atmosphere [42].

3.4. SEM-EDX Analysis. The SEM images of Fe_3O_4 NPs have different morphology as shown in Figures 6(a)–6 (d). The morphology of uncalcined Fe_3O_4 NPs as indicated in Figure 6(a) is not clearly identified. The SEM images of calcined Fe_3O_4 NPs in Figures 6(b)–6 (d) indicate the agglomeration of particles that increases with the concentration of iron salts precursor. The morphology of Fe_3O_4 NPs synthesized from mixture of hydrated ferric and ferrous chloride in different mixing ratio of precursor salt to the plant extract such as 2 : 1, 1 : 1, and 1 : 2 has agglomerated cubic spinel structure.

The scanning electron microscope results confirmed that the grain sizes of the NPs were strongly dependent on mixing ratio of iron salts and leaf extract under the same reaction conditions. The SEM images clearly showed microstructural features and diverse morphologies for Fe_3O_4 nanopowder.

The chemical composition of Fe_3O_4 NPs synthesized in different mixing ratios of precursor salt to the plant extract such as 2 : 1, 1 : 1, and 1 : 2 samples was elucidated by energy-dispersive X-Ray spectroscopy (EDX) (Figure 7). Figure 7(a) reveals the elemental composition of uncalcined Fe_3O_4 NPs, and Figures 7(b)–7(d) depicted EDX spectra of Fe_3O_4 NPs synthesized in 1 : 1, 1 : 2, and 2 : 1 rations, respectively. The EDX spectral intensity in Figure 7 revealed that iron atom has high proportion than oxygen.

The EDX analysis of all the Fe_3O_4 NPs is shown in Figures 7(a)–7(d). It is evident from EDX spectrum of all the samples in which Fe and O are found in the respective spectrum. In addition to that, interestingly it is observed that there was foreign material present in the spectrum. It could be due to the impurity of the samples.

3.5. UV-Vis Analysis. From the data of UV-Vis reflectance spectra of uncalcined and calcined samples of Fe_3O_4 NPs, bandgaps were calculated from Tauc plots shown in Figure 8. Accordingly, the bandgap value of uncalcined Fe_3O_4 NPs was found to be 2.25 eV, and bandgap values of Fe_3O_4 NPs prepared in different salt to the plant extract volume ratios of 1 : 2, 1 : 1, and 2 : 1 were calculated to be 2.35, 2.02, and 2.1 eV which are in agreement with previously reported results [43].

3.6. Adsorption Batch Studies

3.6.1. Optimizer Design of Different Parameters. Since the adsorption efficiency of the sample S11 was higher than the other samples, all the parameter optimizer designs were done on this best sample of Fe_3O_4 NPs for remediation of Cr(VI) and Hg(II). The optimizer design processes of variables were done to get maximum % removal of chromium and mercury. At initial concentration of 20 mg/L, maximum removal of 85% chromium and 95% of mercury was achieved with the Fe_3O_4 NPs by keeping other parameters constant (pH = 5, adsorbent dosage = 300 mg, contact time = 90 min) (Figure 9(a)). At pH 5, 85% of chromium and at pH 7, 85% of mercury removal was achieved (at *Co* = 20 mg/L, contact time = 90 min, and adsorbent dosage = 300 mg). 85% of chromium and 90% of mercury were removed at adsorbent dosage of 700 mg (at *Co* = 20 mg/L, contact time = 90 min, and pH = 5). Removal efficiency for chromium at 60 min was found to be 86% and at 90 min for mercury was found to be 90% by keeping other parameters constant (pH = 5, *Co* = 20 mg/L, and absorbent dosage = 300 mg).

3.6.2. Factors Affecting the Adsorption. It was reported in the past studies that various factors possibly affect the adsorption capacity of nano-adsorbents during the adsorption process. Efficiency of any adsorbent is significantly affected by the physicochemical characteristics of the solutions such as pH value, initial concentration, contact time, and adsorbent dosage. Higher adsorption capacities can be obtained by optimizing the above parameters [44].

(1) (1) Effect of Initial Concentration. The initial solution concentration serves to be the driving force to overcome the mass transfer resistance of metal across the solvent and solid phases [45].

The effect of initial concentrations on adsorption of chromium and mercury ions was investigated from 20 mg/L to 80 mg/L, by keeping all the other parameters constant (at pH = 5, contact time = 90 min, and absorbent dosage =

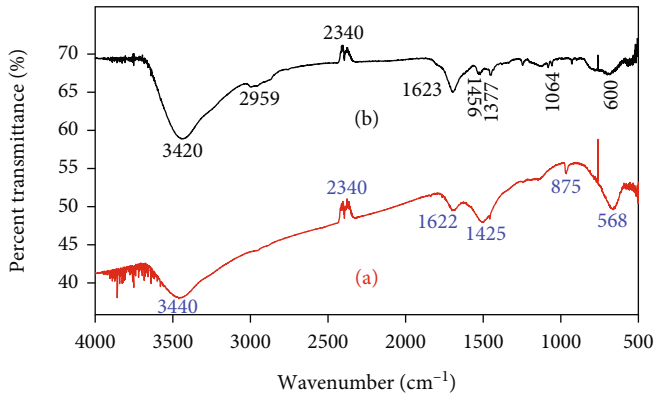

Figure 5: FT-IR spectrum of (a) calcined and (b) uncalcined Fe_3O_4 NPs.

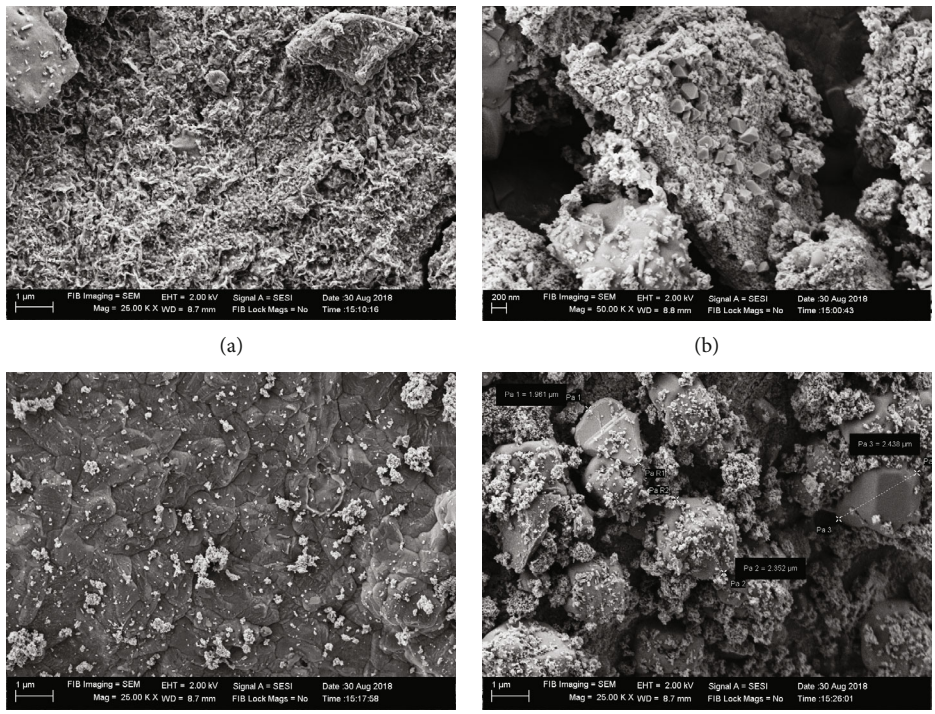

Figure 6: SEM images of Fe_3O_4 NPs: (a) for uncalcined in (1 : 1), (b) for calcined S11 in (1 : 1), (c) for calcined S12 in (1 : 2), and (d) for calcined S21 in (2 : 1).

300 mg). The equilibrium curve (Figure 9(a)) revealed that the overall percentage of removal of Cr(VI) and Hg(II) from the solution was found to decrease with an increase in the initial of concentration Cr(VI) and Hg(II). This could be justified by the fact that, with the increase in the concentration of Cr(VI) or Hg(II) in solution with a fixed amount of adsorbent, binding capacity of adsorbent is believed to approach to the saturation point resulting in decrease in both Cr(VI) and Hg(II) removal. At higher Cr(VI) and Hg(II) concentration; the number of active sites on adsorbent surface is not enough to accommodate both chromium and mercury ions; however, at low concentration, the ratio of surface active sites to total concentration of Cr(VI) and Hg(II) was high and therefore the two metal ions were found to interact effectively with the active sites on adsorbent surface sufficiently [46].

(2) (2) Effect of Adsorbent Dosage. Figure 9(b) presents a fact that the percentage removal of Cr(VII) and Hg(II) ions was found to increase with an increase in the amount of adsorbent dosage. This observation clearly indicates that the number of available adsorption sites influences removal efficiency. Metal ion adsorption efficiency by adsorbent was found to increase with the increase in adsorbent dose.

(3) (3) Effect of Contact Time. The adsorption experiments were conducted for various contact times with the fixed values for the other factors, sorbent dose, pH, and initial

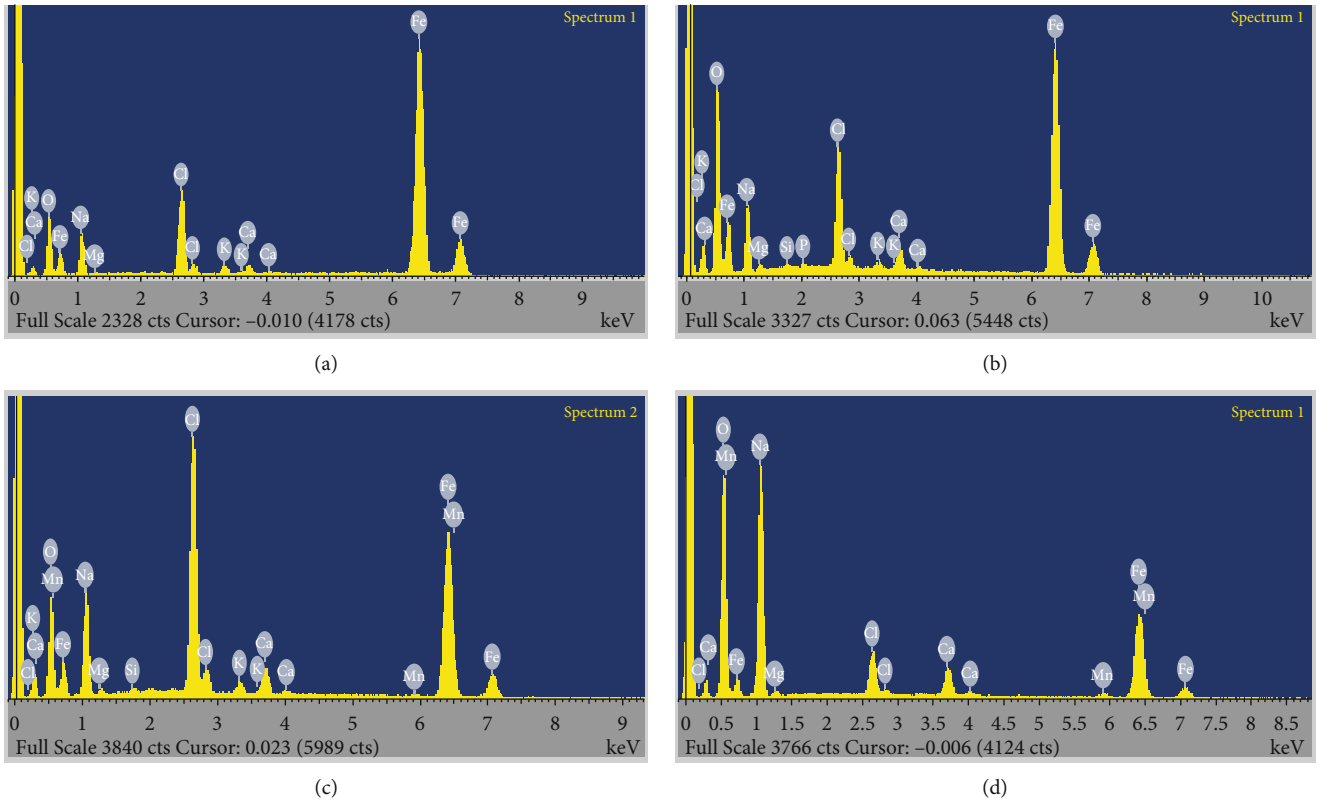

Figure 7: EDX spectra of Fe_3O_4 NPs: (a) for uncalcined sample S11 in (1 : 1), (b) for calcined sample S11 in (1 : 1), (c) for calcined sample S12 in (1 : 2), and (d) for calcined S21 in (2 : 1).

concentration. These results are depicted in Figure 9(c). It reveals that the removal efficiency of chromium and mercury by the adsorbent was found to increase in the beginning but later continues to increase at a relatively slower rate with contact time until equilibrium is reached. Generally, the rate of removal of adsorbate appears to be rapid initially, but after saturation of removal efficiency at optimum contact time, the trend of percent removal efficiency for both metal ions slightly declines with time. As shown in Figure 9(c), the optimum equilibration time (contact time) for adsorption of Cr(VI) ion was 60 min and for that of Hg(II) ion was 90 min at percent removal efficiency for 86% and 90%, respectively.

(4) (4) Effect of pH on Adsorption. The pH of the solution affects both the degree of dissociation of functional groups from the adsorbent surface and the solubility of the metal ions. The various species of Hg(II) and Cr(VI) are greatly dependent on the pH of the solution [47], and pH values from 3 to 11 were selected for the experimentation. The obtained results (Figure 9(d)) showed that the removal of metal ions was strongly influenced by the pH of the solution. The removal efficiency of adsorbent Fe_3O_4 NPs was increased from pH 3 to 5 for chromium ion and 3 to 7 for mercury ion. Fe_3O_4 NPs exhibited the highest percent removal of chromium (VI) at pH value of 5 and of mercury at pH value of 7, respectively. At low pH conditions (pH<5), the active surface sites of Fe_3O_4 NPs adsorbent were protonated [48], lowering the adsorption of heavy metal ions (chromium ions and mercury ions) as there is competition between H^+ ions and metal ions. Metal ion removal of Fe_3O_4 NPs remains significantly high beyond optimum values of pH (at pH>7), as there was electrostatic interaction between metal ions and negatively charged surface of the adsorbed, and also because of hydrolysis of metal ions at higher pH [49].

Percent removal efficiency (%R) and adsorption capacities (q) of Fe_3O_4 NPs for removal of Hg(II) and Cr(VI) ions in wastewater against pH and contact time are summarized in Table 1. As shown in Table 1, both %R and adsorption capacity values were increased with increasing the contact time up to maximum removal efficiency of 90% and maximum adsorption capacity (qm) of 60 mg/g at contact time of 90 minute for Hg(II) and in the same way, %R and adsorption capacity were increased up to maximum removal efficiency of 86% and maximum adsorption capacity of 57.37 mg/g with increase in contact time up to 90 minute for Cr(II), respectively. Increasing the contact time beyond 90 minute for both Hg(II) and Cr(VI) results in decreasing removal efficiency and adsorption capacity. As depicted in Table 1, percent removal efficiency (%R) and adsorption capacity of Fe_3O_4 NPs for removal of Hg(II) and Cr(VI) ions in wastewater against pH show maximum %R value (85%) and g (56.66 mg/g) for Hg(II) (at pH =7), and maximum percent removal value (85%) and maximum adsorption

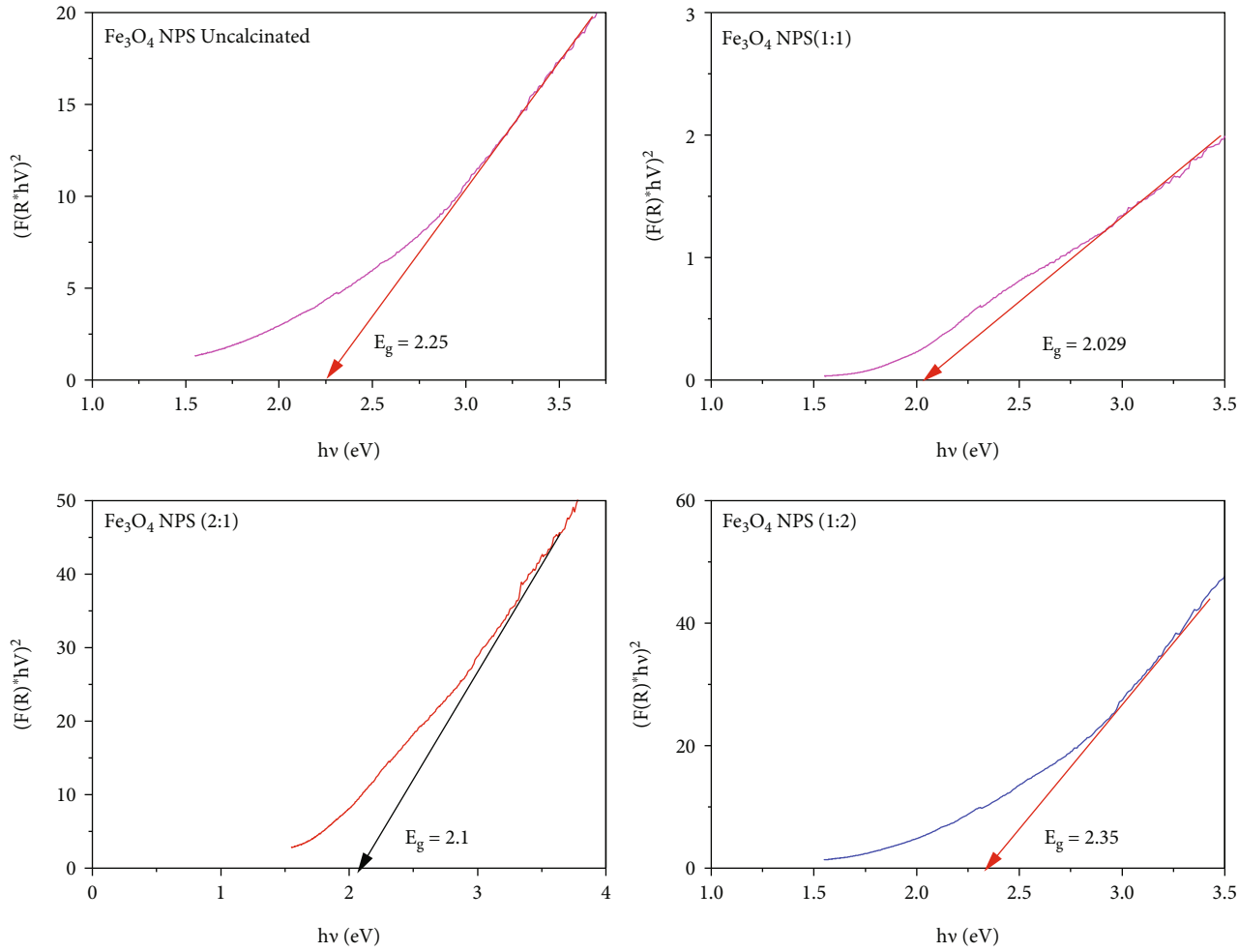

Figure 8: Tauc plots and the bandgaps of uncalcined and calcined samples of (S11), (S12), and (S21) Fe_3O_4 NPs.

capacity (56.66 mg/g) for Hg(II) (at pH = 5), respectively. Based on the data of Figure 9(a), at lower initial concentration (20 mg/L), maximum percent removal efficiency of 95% for Hg(II) and 86% for Cr(VI) were observed. Correspondingly, maximum adsorption capacity of Fe_3O_4 NPs was extracted from the same figure to be 63.33 mg for Hg(II) and 56.61 mg/g for Cr(VI).

3.7. Sorption Kinetics Studies. The kinetics of sorption of Cr(VI) and Hg(II) on the surface of Fe_3O_4 NPs was investigated against pseudo-first-order and pseudo-second-order models (Figure 2s in supplementary section and Table 2). From the values of R^2, the data of adsorption of Cr(VI) and Hg(II) was found to fit well with pseudo-second-order models (Table 2).

The degree of goodness of linear fit in kinetic models can be judged from the value of rate constants and R^2. Table 2 presents the kinetic rate constants of pseudo-first-order and pseudo-second-order models. The pseudo-second-order kinetics present the high correlation coefficients than pseudo-first-order for both Hg(II) and Cr(VI) adsorptions, and the experimental q_e values obtained are closer to those calculated for the pseudo-second-order kinetic model.

3.8. Sorption Isotherm Studies. To evaluate the mechanism of uptake of Hg(II) and Cr(VI) ions in wastewater on to the surface of Fe_3O_4 NPs, the Langmuir and Freundlich adsorption isotherm models were employed to analyze the adsorption data (Figure 3s in supplementary section).

K_f and n are parameters characteristic of the sorbent-sorbate system, which were determined by data fitting and whereas linear regression was determined from the fits of the kinetic and isotherm models [50].

Table 3 summarizes the Langmuir and Freundlich isotherm models for both Cr(VI) and Hg(II) adsorption. The values of isotherm parameters, $1/n = 0.483$ (at $n = 2.07$), indicating that the sorption of Cr(VI) unto the magnetic adsorbent was favorable with R^2 value of 0.9814.

From the data of Table 3, the values of isotherm parameters, $1/n = 0.294$ (at $n = 3.40$), indicating that the sorption of Hg(II) unto the magnetic adsorbent of Fe_3O_4 NPs was favorable with R^2 value of 0.967. Based on information obtained from value of $R^2 = 0.90$ for Cr(VI) sorption and from value of $R^2 = 0.9741$ for Hg(II) using the Langmuir isotherm model, sorption of Hg(II) best fits with the Langmuir isotherm than Cr(VI). In the same way, the sorption of Cr(VI) best fits with the Freundlich isotherm than Hg(II) does.

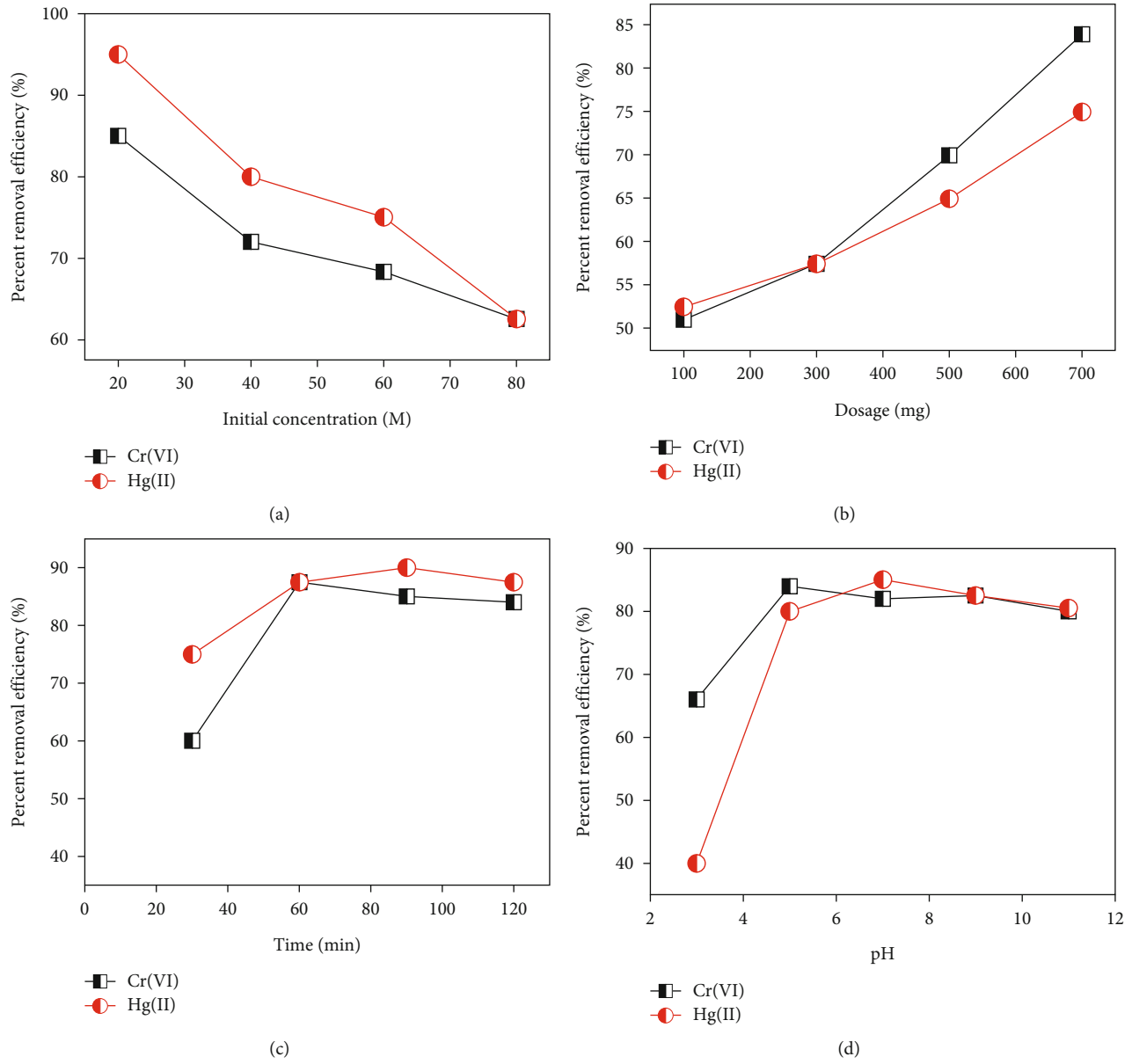

Figure 9: Influence of initial concentration of Cr(VII) and Hg(II) (a). Dosage of adsorbent (b), contact time (c), and pH (d) of the solution medium on the percent removal efficiency of Fe_3O_4 NPs on heavy metals (Cr(VII), and Hg(II)).

Table 1: Summary of parameters such as pH and contact time on percent removal efficiency and adsorption capacity of Fe_3O_4 NPs in removing Hg(II) and Cr(VI) ions from wastewater.

pH	Hg(II)		Cr(VI)		Contact time (min)	Hg(II)		Cr(VI)	
	%R	q (mg/g)	%R	q (mg/g)		%R	q (mg/g)	%R	q (mg/g)
3	40	26.66	66	44.00	30	75	50.00	60	40.00
5	80	53.33	85	56.66	60	87.5	58.33	86	57.33
7	85	56.66	82	54.66	90	90	60.00	85	56.66
9	82.5	55.00	82.5	55.00	120	87.5	58.33	84	56.66
11	80	53.33	82	55.00					

Table 3 shows a summary of the Langmuir and Freundlich isotherm model constants and correlation coefficients for the adsorption of chromium and mercury [51].

3.9. FT-IR Analysis before and after Adsorption of Hg(II) and Cr(VI). FT-IR spectral of synthesized Fe_3O_4 NPs (adsorbent) before and after adsorption (loading) of Cr(VI) and Hg(II)

Table 2: The adsorption kinetic model rate constants for adsorption of chromium and mercury.

Metal ions	Pseudo 1st order kinetic model			Pseudo 2nd order kinetic model		
	q_e	K_1	R^2	q_e	K_2	R^2
Cr(VI)	2.11	-7.00E^{-4}	0.2391	1.36	0.057	0.9750
Hg(II)	1.95	-5.33E-4	0.32	1.33	0.142	0.9944

Table 3: Langmuir and Freundlich isotherm model constants and correlation coefficients for adsorption of chromium and mercury.

Isotherms	Cr(VI)		Hg(II)	
	R^2	Estimated isotherm parameters	R^2	Estimated isotherm parameter
Langmuir	0.90	Q_o (mg/g) =0.951 K_L (L/mg) =0.078	0.9741	Q_o (mg/g) = 2.631 K_L (L/mg) = 0.287
Freundlich	0.9814	K_f =1.614 n =2.07	0.967	K_f =3.16 n =3.40

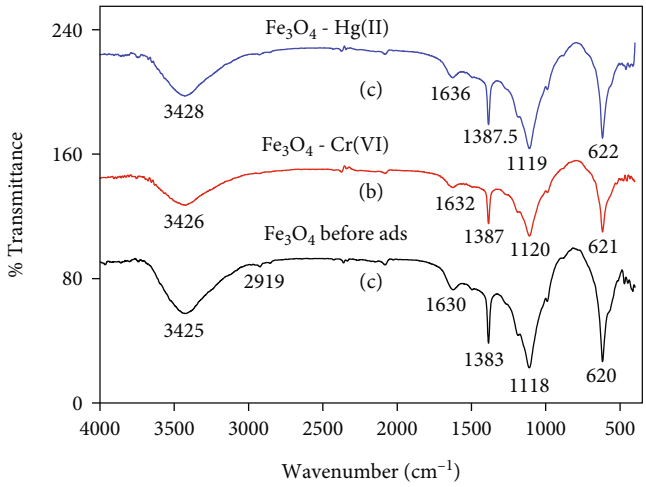

Figure 10: FT-IR spectra of green synthesized Fe_3O_4 Nanostructures (a) before and (b) after adsorption of Cr(VI) and (c) Hg(II), respectively.

heavy metal ions was recorded and shown in Figure 10. The FT-IR spectra of Fe_3O_4 NPs after adsorption of Cr(VI) and Hg(II) metal ions have shown various functional groups, and slight peak shifts. In Figure 10, the peaks at 3425, 1630, 1383, and 1118 cm^{-1} shifted towards the peak at 3426, 1632, 1387, and 1120 cm^{-1}, respectively, for Cr(VI) ion adsorption, and shifted to the peaks at 3428, 1636, 1387.5, and 1119 cm^{-1} for Hg(II) ion adsorptions. Small peak at 2959 has been disappeared and the hydroxyl peak at around 1630 cm^{-1} shifted to 1632 cm^{-1} and to 1636 cm^{-1} after adsorption of Cr(VI) and Hg(II) ions, respectively. The peak intensity reduction and peak shift has been also shown after adsorption of Hg(II) onto Fe_3O_4 nanostructures [52].

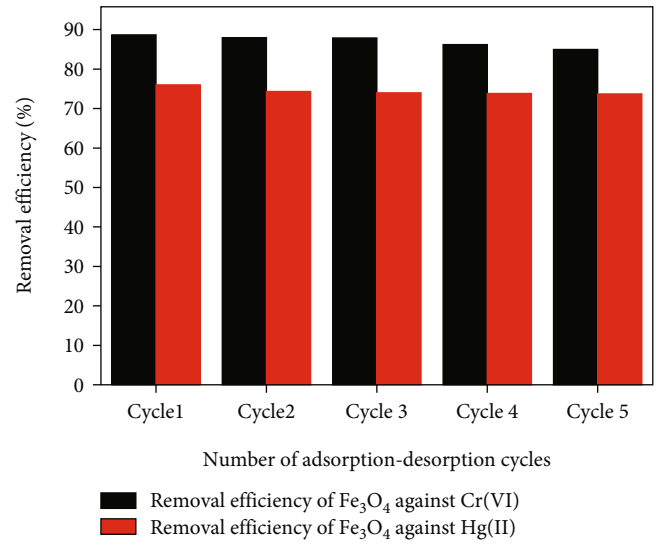

Figure 11: Regeneration study of synthesized Fe_3O_4 nanoparticle for adsorptive removal of Hg(II) and Cr(VI) meta-ions in wastewater.

The peak at around 1118 cm^{-1} attributed to (–C-O) bond stretching in thymol and carvacrol phytochemicals extracted from *Thymus schimperi*; and the peak due to the hydroxyl group at 1632 cm^{-1} has decreased after adsorption of Cr(VI) (Figure 10(b)), and at 1636 after adsorption of Hg(II) (Figure 10(c)). The intense peaks at around 1118 cm^{-1} (due to C-O functional group of the plant extracts) and at around 1405 cm^{-1} (due to carboxylic functional groups) have been decreased after adsorption of Cr(VI) (Figure 10(b)) and Hg(II) (Figure 10(c)). These changes in the absorption peaks indicated that the active sites on the surface of Fe_3O_4 nanostructures contained hydroxyl, ketonic, and carboxylic functional groups, which formed new chemical bonds with Hg(II) and Cr(VI) ions [53]. The presence of intense band between 650 and 550 cm^{-1} is due to Fe-O bond vibration in Fe_3O_4 NPs [39]. This further confirms the mechanism of adsorption evaluated using adsorption kinetic and isotherm models.

3.10. Regeneration Study. For a cost-effective magnetite nano-adsorbent, Fe_3O_4 NPs, it was essential to study the reusability or recyclability in repeated use for removal of Hg(II) and Cr(VII) ions from wastewater. Magnetic iron oxide (Fe_3O_4) NPs have been applied in adsorptive removal of metallic ions from contaminated water and recovered back for repeated use [54, 55].

For example, Rivera et al. studied Cr(VI) ion removal using 2 g/L of the magnetic magnetite NP [56].

The regenerations study for adsorption-desorption of Hg(II) ions using synthesized Fe_3O_4 NPs in wastewater was done at optimum initial concentration of 20 mg/l, contact time of 60 minutes, and with 30 mg of Fe_3O_4 NPs in 100 ml volumetric flask. The same procedures were followed for adsorption-desorption of Cr(VI) against Fe_3O_4 NPs at the optimum pH of 5 and contact time of 90 minutes. In the process of loading and elution of Hg(II) and Cr(VI) ions

Table 4: Maximum sorption efficiencies (%R) and sorption capacities (q_m) of magnetite iron oxide nanoparticles and related adsorption parameters for removal of Cr(VI) and Hg(II) ions from wastewater.

S.no	Adsorbate	Adsorbent material	Maximum adsorption capacity (q_m, mg/g)	Removal efficiency (%R)	pH of solution	Temperature (°C)	Adsorption kinetics	Adsorption isotherm	References
1	Hg(II)	Fe_3O_4 NPs	NA	87	5.5	25	PSO	Freundlich	[59]
2	Hg(II)	Fe_3O_4 NPs	NA	43.74	6	25	PSO	Langmuir	[59]
3	Cr(VI)	Fe_3O_4 NPs	105.26	82	5.2	25	PSO	Langmuir	[61]
4	Cr(VI)	Fe_3O_4 NPs	NA	72.45		25	PSO	Freundlich	[62]
5	Cr(VI)	Fe_3O_4 NPs	NA	98.95	2	25	PSO	Langmuir	[63]
6	Cr(VI)	Fe_3O_4 NPs	26.5	NA	2	25	PSO	Freundlich	[64]
7	Cr(VI)	Fe_3O_4 NPs	15	NA	1	25	PFO	Langmuir	[52]
8	Hg(II)	Schiff base decorated PAMAM dendrimer/ Fe_3O_4 composites	605.78	NA	6	25	PSO	Langmuir	[13]
9	Hg(II)	Sulfur-functionalized PAMAM dendrimer/ Fe_3O_4 composites	160.47	NA	6	25	PSO	Langmuir	[14]
10	Cr(VI)	Fe_3O_4 NPs	8.67	NA	4	25	PSO	Langmuir	[65]
11	Hg(II)	Fe_3O_4 NPs	63.33	95	7	27	PSO	Langmuir	This study
	Cr(VI)	Fe_3O_4 NPs	56.61	86	5	27	PSO	Freundlich	

N.B: PFO = pseudo first order; PSO = pseudo second order; PAMAM = polyamidoamine; NA = not available.

to and from Fe_3O_4 NPs, the elution operations were carried out by shaking the Hg(II) adsorbed and Cr(VI) adsorbed Fe_3O_4NPs with 0.50 M HCl in 100 ml volumetric flask separately. The regeneration of the nanoparticles was done for multiple adsorption-desorption cycles. The recycled Fe_3O_4 NP were tested against removal of Hg(II) and Cr(VI) metal ions for 1st, 2nd, 3rd, 4th, and 5th cycles, respectively(Figure 4s and Figure 5s in supplementary section). The data of the regeneration study of Fe_3O_4 NP against Hg(II) and Cr(VI) metal ions for the 1st five cycles are shown in Figure 11.

The regeneration cycles of the magnetic nanomaterials showed a slight decrease (about 4.17% for Cr(VI) and 3% for Hg(II) ions) in the removal efficiency between the 1st cycle and 5th cycle, indicating that the nanomaterial was reused for up to 5 cycles sequentially without significant reduction in removal efficiency of Fe_3O_4 NPs against Hg(II) and Cr(VI) metal ions. This finding is in line with previous reports in regeneration study for magnetite and magnetite-based nanostructures [3, 56–58] for the similar heavy metal ions.

Maximum removal efficiency (%R), maximum adsorption capacity (q_m), optimum pH, working temperature of solution medium, kinetics, and adsorption isotherms for sorption of Hg(II) and Cr(VI) onto synthesized Fe_3O_4 NPs are collected in Table 4. The comparative data for removal efficiency (%R), maximum adsorption capacity (q_m), and other adsorption conditions of Fe_3O_4 nanoparticles and Fe_3O_4-based nanocomposites for Hg(II) and Cr(VI) sorption are summarized in Table 4. The percent removal efficiency (%R) of synthesized Fe_3O_4 NPs in this study for adsorption of Hg(II) is in agreement with reported value by Zaki et al. [59], and is higher than other reported values by [60, 61]; and % R for adsorption of Cr(VI) in this study is higher than reported value by [62] whereas it is lower than the reported value by [63]. Obtained maximum adsorption capacity (q_m) for Cr(VI) (56.61 mg/g) and Hg(II) (63.33 mg/g) is in between the maximum value from by Y. Zhou et al., L. Luan et al., and H. Kumar et al. and other related minimum q_m values reported in [64, 65].

Schiff-based functionalized polyamidoamine (PAMAM) dendrimer composites of Fe_3O_4 NPs and sulfur-functionalized PAMAM dendrimer/Fe_3O_4 nanocomposite materials were studied to decontaminate aqueous Hg(II) by Y. Zhou et al. [65], and by L. Luan et al. [14] and the maximum adsorption capacity of 605.78 mg/g and 160.47 mg/g, respectively, was achieved. In other related reports, magnetite Fe_3O_4 NPs were used to remove Cr(VI) ion from wastewater at initial concentration of adsorbate of 2 g/d m^3 and at pH =4, and with maximum adsorption capacity of 8.67 mg/g was achieved [65].

From the data of adsorption kinetics, adsorption isotherms, and FT-IR analysis before and after adsorption of the heavy metal ions onto Fe_3O_4 NPs, the upload of Hg(II) and Cr(VI) ion by the magnetite iron oxide NPs is dominated by the chemical interaction between adsorbent (Fe_3O_4 NPs) and adsorbate (Hg(II) and Cr(VI)).

4. Conclusion

The XRD study revealed that the phase structure of Fe_3O_4 NPs were cubic face centered with average crystallite size between 20 and 30 nm. The SEM micrographs depicted the

agglomerated grain size of synthesized Fe_3O_4 NPs. The maximum percent removal efficiency of the adsorbent material (Fe_3O_4 NPs) for adsorption of chromium (VI) was 86% (at initial concentration of 20 mg/L, contact time of 90 min, and adsorbent dose of 300 mg) and for mercury (II) 90% (at initial concentration of 20 mg/L, and contact time of 90 min) from aqueous polluted water. At pH =7, the percent removal efficiency of Fe_3O_4 NPs to adsorb Hg(II) was 90% (at constant time of 90 min, initial concentration of 20 mg/L, and adsorbent dose of 300 mg); at pH =5, the percent removal efficiency of Fe_3O_4 NPs to adsorb Cr(VI) ion was 86% (at constant time of 60 min, initial concentration of 20 mg/L, and adsorbent dose of 300 mg). The mechanism of both Hg(II) and Cr(VI) metal ion adsorptions was best fitted with pseudo-second-order kinetics, and Cr(VI) ion sorption follows the Freundlich adsorption isotherm model whereas Hg(II) ion sorption fitted with the Langmuir isotherm model. The regenerability study of the adsorbent material (Fe_3O_4 NPs) performed for five consecutive cycles shows only slight decrease in removal efficiency (4.17% for Cr(VI) and 3% for Hg(II)) between the 1st and the 5th adsorption-desorption cycle.

Data Availability

The data of FT-IR spectra, XRD Analysis, SEM-EDX, TGA-DTA, and kinetic study used to support the findings of this study are included within the article; and also can be released from the corresponding author upon request to the Hindawi (Journal of Nanomaterials).

Conflicts of Interest

There are no potentially available conflicts of interest, authorship, and/or publication of this article.

Acknowledgments

I (F. K. Sabir) and S. T. Geneti (my student who used this work as his M,Sc. Thesis) greatly acknowledged Adama Science and Technology University (ASTU) for providing financial support through ASTU's 12th cycle research grant successfully. The authors extend their thanks to the Department of Applied Chemistry and Department of Materials Science and Engineering at ASTU for providing facilities such as TGA-DTA analyzer and XRD setup. Department of Chemistry at Addis Ababa University was also thanked by the authors for allowing FT-IR characterization. The authors also acknowledged East West Institute of Technology (India) for SEM-EDX and UV-Visible reflectance analysis.

Supplementary Materials

Supplementary section has included five figure data (Figure 1s–Figure 5s). The photograph of the plant used in synthesis of Fe_3O_4 NPs (*Thymus schimperi*) is given by Figure 1s. The plots of pseudo-first and pseudo-second-order kinetic models for adsorption of Hg(II) and Cr(VI) metal ions onto Fe_3O_4 NPs are shown by Figure 2s. The plots of the Freundlich and Langmuir adsorption isotherm models are shown in Figure 3s. The basic data for regeneration study is given by Figures 4s and 5s. The UV-Vis absorbance spectra of Cr(VI) and Hg(II) metal ions for five sequential cycles of adsorption–desorption phenomena were depicted by Figure 4s and Figure 5s, respectively. *(Supplementary Materials)*

References

[1] K. Parajuli, A. K. Sah, and H. Paudyal, "Green synthesis of magnetite nanoparticles using aqueous leaves extracts of <i>Azadirachta indica</i> and its application for the removal of As(V) from water," *Green and Sustainable Chemistry*, vol. 10, no. 4, pp. 117–132, 2020.

[2] H. T. Ha, N. T. Huong, L. L. Dan, N. D. Tung, V. B. Trung, and T. D. Minh, "Removal of heavy metal ion using polymer-functionalized activated carbon: aspects of environmental economic and chemistry education," *Journal of Analytical Methods in Chemistry*, vol. 2020, 13 pages, 2020.

[3] R. Kumar, P. Rauwel, and E. Rauwel, "Nanoadsorbants for the removal of heavy metals from contaminated water: current scenario and future directions," *PRO*, vol. 9, no. 8, pp. 1379–1408, 2021.

[4] B. E. Igiri, S. I. R. Okoduwa, G. O. Idoko, E. P. Akabuogu, A. O. Adeyi, and I. K. Ejiogu, "Toxicity and bioremediation of heavy metals contaminated ecosystem from tannery wastewater: a review," *Journal of Toxicology*, vol. 2018, 16 pages, 2018.

[5] T.-K. Tran, H.-J. Leu, K.-F. Chiu, and C.-Y. Lin, "Electrochemical treatment of heavy metal-containing wastewater with the removal of COD and heavy metal ions," *Journal of the Chinese Chemical Society*, vol. 64, no. 5, pp. 493–502, 2017.

[6] Z. Chen, B. Tang, Y. Niu et al., "Synthesis of silica supported thiosemicarbazide for Cu(II) and Zn(II) adsorption from ethanol: a comparison with aqueous solution," *Fuel*, vol. 286, pp. 119287–119295, 2021.

[7] H. T. Kara, S. T. Anshebo, and F. K. Sabir, "Preparation and characterization of functionalized cellulose nanomaterials (CNMs) for Pb(II) ions removal from wastewater," *Journal of Chemistry*, vol. 2021, 18 pages, 2021.

[8] H. T. Kara, S. T. Anshebo, F. K. Sabir, and G. A. Workineh, "Removal of methylene blue dye from wastewater using periodiated modified nanocellulose," *International Journal of Chemical Engineering*, vol. 2021, 6 pages, 2021.

[9] Z. Cheng, A. L. K. Tan, Y. Tao, D. Shan, K. E. Ting, and X. J. Yin, "Synthesis and characterization of iron oxide nanoparticles and applications in the removal of heavy metals from industrial wastewater," *International Journal of Photoenergy*, vol. 2012, 5 pages, 2012.

[10] A. M. Gutierrez, T. D. Dziubla, and J. Z. Hilt, "Recent advances on iron oxide magnetic nanoparticles as sorbents of organic pollutants in water and wastewater treatment," *Reviews on Environmental Health*, vol. 32, no. 1-2, pp. 111–117, 2017.

[11] M. Gui, V. Smuleac, L. E. Ormsbee, D. L. Sedlak, and D. Bhattacharyya, "Iron oxide nanoparticle synthesis in aqueous and membrane systems for oxidative degradation of trichloroethylene from water," *Journal of Nanoparticle Research*, vol. 14, no. 5, pp. 861–877, 2012.

[12] G. Yirga, H. C. A. Murthy, and E. Bekele, "Synthesis and characterization of humic acid-coated Fe_3O_4 nanoparticles for

methylene blue adsorption activity," *Advanced Materials Letters*, vol. 10, no. 10, pp. 715–723, 2019.

[13] Y. Zhou, L. Luan, B. Tang et al., "Fabrication of Schiff base decorated PAMAM dendrimer/magnetic Fe_3O_4 for selective removal of aqueous Hg(II)," *Chemical Engineering Journal*, vol. 398, article 125651, 2020.

[14] L. Luan, B. Tang, Y. Liu et al., "Selective capture of Hg(II) and Ag(I) from water by sulfur-functionalized polyamidoamine dendrimer/magnetic Fe_3O_4 hybrid materials," *Separation and Purification Technology*, vol. 257, article 117902, 2021.

[15] K. Mittal, Y. Chisti, and U. C. Banerjee, "Synthesis of metallic nanoparticles using plant extracts," *Biotechnology Advances*, vol. 31, no. 2, pp. 346–356, 2013.

[16] W. S. W. Ngah and M. A. K. M. Hanafiah, "Removal of heavy metal ions from wastewater by chemically modified plant wastes as adsorbents: review," *Biotechnology*, vol. 99, pp. 3935–3948, 2008.

[17] T. B. Asfaw, T. M. Tadesse, and A. M. Ewnetie, "Determination of total chromium and chromium species in Kombolcha tannery wastewater, surrounding soil, and lettuce plant samples, South Wollo, Ethiopia," *Advances in Chemistry*, vol. 2017, 7 pages, 2017.

[18] G. K. Kinuthia, V. Ngure, D. Beti, R. Lugalia, A. Wangila, and L. Kamau, "Levels of heavy metals in wastewater and soil samples from open drainage channels in Nairobi, Kenya: community health implication," *Scientific Reports*, vol. 10, no. 1, pp. 8434–8844, 2020.

[19] H. Khademi, M. Gabarron, A. Abbaspour, S. Martinez-Martinez, A. Faz, and J. A. Acosta, "Environmental impact assessment of industrial activities on heavy metals distribution in street dust and soil," *Chemosphere*, vol. 217, pp. 695–705, 2019.

[20] H. T. Kara, S. T. Anshebo, and F. K. Sabir, "A novel modified cellulose nanomaterials (CNMs) for remediation of chromium (VI) ions from wastewater," *Materials Research Express*, vol. 7, no. 11, article 115008, 2020.

[21] WHO (2003), *Chromium in drinking-water. Background document for preparation of WHO Guidelines for drinking-water quality*, World Health Organization (WHO/SDE/WSH/03.04/4), Geneva, 4th edition edition, 2017.

[22] J. Mateo-Sagasta, S. M. Zadehand, H. Turral, and IWMI & FAO, *Water pollution from agriculture: a global review*, 2017.

[23] A. Nigist, H. J. Storesund, L. Skattebol, F. Tonnesen, and A. J. Aasen, "Volatile oil constituents of twoThymus species from Ethiopia," *International Journal of Science*, vol. 15, no. 2, pp. 123–125, 2000.

[24] M. Sravanthi, D. MuniKumar, M. Ravichandra, G. Vasu, and K. P. J. Hemalatha, "Green synthesis and characterization of iron oxide nanoparticles using Wrightia tinctoria leaf extract and their antibacterial studies," *International Journal of Current Research Academic Review*, vol. 4, no. 8, pp. 30–44, 2016.

[25] E. T. Bekele, E. A. Zereffa, N. S. Gultom, D.-H. Kuo, B. A. Gonfa, and F. K. Sabir, "Biotemplated synthesis of titanium oxide nanoparticles in the presence of root extract of Kniphofia schemperi and its application for dye sensitized solar cells," *International Journal of Photoenergy*, vol. 2021, 12 pages, 2021.

[26] E. T. Bekele, B. A. Gonfa, O. A. Zelekew, H. H. Belay, and F. K. Sabir, "Synthesis of titanium oxide nanoparticles using root extract of Kniphofia foliosa as a template, characterization, and its application on drug resistance bacteria," *Journal of Nanomaterials*, vol. 2020, 10 pages, 2020.

[27] N. Ajinkya, X. Yu, P. Kaithal, H. Luo, P. Somani, and S. Ramakrishna, "Magnetic iron oxide nanoparticle (IONP) synthesis to applications: present and future," *Materials*, vol. 13, no. 20, p. 4644, 2020.

[28] M. A. J. Kouhbanani, N. Beheshtkho, A. M. Amani et al., "Green synthesis of iron oxide nanoparticles using Artemisia vulgarisleaf extract and their application as a heterogeneous Fenton-like catalyst for the degradation of methyl orange," *Materials Research Express*, vol. 5, no. 11, article 115013, 2018.

[29] A. M. Awwad and N. M. Salem, "A Green and facile approach for synthesis of magnetite nanoparticles," *Journal of Nanoscience and Nanotechnology*, vol. 2, no. 6, pp. 208–213, 2012.

[30] Z. Chen, T. Wang, X. Jin, M. Megharaj, and R. Naidu, "Multifunctional kaolinite-supported nanoscale zero-valent iron used for the adsorption and degradation of crystal violet in aqueous solution," *Journal of Colloid and Interface Science*, vol. 398, pp. 59–66, 2013.

[31] N. Basavegowda, K. B. S. Magar, K. Mishra, and Y. R. Lee, "Green fabrication of ferromagnetic Fe_3O_4 nanoparticles and their novel catalytic applications for the synthesis of biologically interesting benzoxazinone and benzthioxazinone derivatives," *Journal of Chemimstry*, vol. 38, pp. 5415–5420, 2014.

[32] K. S. Padmavathy, G. Madhu, and P. V. Haseena, "A study on effects of pH, adsorbent dosage, time, initial concentration and adsorption isotherm study for the removal of hexavalent chromium (Cr (VI)) from wastewater by magnetite nanoparticles," *International Conference Engineering, Science and Technology*, vol. 24, pp. 585–594, 2016.

[33] A. Mohd, R. Sumbul, A. Masood, and P. Arulazhagan, "Adsorption of Hg(II) from Aqueous Solution Using Adulsa (Justicia adhatoda) Leaves Powder: Kinetic and Equilibrium Studies," *Journal of Chemistry*, vol. 2013, 11 pages, 2013.

[34] K. K. Onchoke and S. A. Sasu, "Determination of hexavalent chromium (Cr(VI)) concentrations via ion chromatography and UV-Vis spectrophotometry in samples collected from Nacogdoches Wastewater Treatment Plant, East Texas (USA)," *Advances in Environmental Chemistry*, vol. 2016, 10 pages, 2016.

[35] H. M. F. Freundlich, "Über die adsorption in Lösungen," *Journal of Physical Chemistry*, vol. 57U, no. 1, pp. 385–470, 1907.

[36] M. Herlekar and S. Barve, "Calcination and microwave assisted biological synthesis of iron oxide nanoparticles," *International Research Journal of Environmental Science*, vol. 4, pp. 28–36, 2015.

[37] H. E. Ghandoor, H. M. Zidan, M. H. K. Mostafa, and M. I. M. Ismail, "Synthesis and some physical properties of magnetite (Fe3O4) nanoparticles," *International Journal of Electrochemical Science*, vol. 7, pp. 1–12, 2012.

[38] N. Sanpo, C. C. Berndt, C. Wen, and J. Wang, "Transition metal-substituted cobalt ferrite nanoparticles for biomedical applications," *Acta Biomaterialia*, vol. 9, no. 3, pp. 5830–5837, 2013.

[39] M. Gotic, T. Jurkin, and S. Music, "Iron (III) precursor to magnetite and vice versa," *Materials Research Bulletin*, vol. 44, no. 10, pp. 2014–2021, 2009.

[40] T. Abera, E. Debebe, R. Ashebir et al., "Phytochemical constituents, safety and efficacy study of Thymus schimperi and Thymus serrulatus," *Journal of Clinical and Experimental Pharmacolology*, vol. 9, no. 5, pp. 1–7, 2019.

[41] F. B. G. Camara, L. A. Costa, G. P. Fidelis et al., "Heterofucans from the brown seaweed Canistrocarpus cervicornis with anticoagulant and antioxidant activities," *Marine Drugs*, vol. 9, no. 1, pp. 124–138, 2011.

[42] C. Yang and C. Wöll, "IR spectroscopy applied to metal oxide surfaces: adsorbate vibrations and beyond," *Advances in Physics: X*, vol. 2, no. 2, pp. 373–408, 2017.

[43] L. Guo, Q. Huang, X. Li, and S. Yang, "Iron oxide nanoparticles synthesis and applications in surface enhanced raman scattering and electrocatalysis," *Physical Chemistry*, vol. 3, pp. 1661–1665, 2001.

[44] M. Hua, S. Zhang, B. Pan, W. Zhang, L. Lv, and Q. Zhang, "Heavy metal removal from water/wastewater by nanosized metal oxides: A review," *Journal of Hazardous Materials*, vol. 211-212, pp. 317–331, 2012.

[45] H. I. Adegoke, F. AmooAdekola, O. S. Fatoki, and B. J. Ximba, "Adsorption of Cr(VI) on synthetic hematite (α-Fe_2O_3) nanoparticles of different morphologies," *Korean Journal of Chemical Engineering*, vol. 31, no. 1, pp. 142–154, 2014.

[46] A. Y. Orbak and I. Orbak, "Effective Factor Analysis for Chromium(VI) Removal from Aqueous Solutions and Its Application to Tunçbilek Lignite Using Design of Experiments," *Journal of Chemistry*, vol. 2019, 10 pages, 2019.

[47] R. Ansari and N. K. Fahim, "Application of polypyrrole coated on wood sawdust for removal of Cr(VI) ion from aqueous solutions," *Reactive and Functional Polymers*, vol. 67, no. 4, pp. 367–374, 2007.

[48] B. N. Pham, J.-K. Kang, C.-G. Lee, and S.-J. Park, "Removal of heavy metals (Cd^{2+}, Cu^{2+}, Ni^{2+}, Pb^{2+}) from aqueous solution using Hizikia fusiformis as an algae-based bioadsorbent," *Applied Sciences*, vol. 11, no. 18, pp. 8604–8616, 2021.

[49] A. A. Naef Qasem, R. H. Mohammed, and D. U. Lawal, "Removal of heavy metal ions from wastewater: a comprehensive and critical review," *Nature Partner Journals Clean Water*, vol. 4, no. 1, pp. 1–15, 2021.

[50] B. Abebe, H. C. A. Murthy, and A. Enyew, "Summary on adsorption and photocatalysis for pollutant remediation: mini review," *Journal of Encapsulation and Adsorption Sciences*, vol. 8, no. 4, pp. 225–255, 2018.

[51] K. S. Somit, H. C. Ananda, and S. V. Murthy, "Adsorption of mercury from aqueous solution using gum acacia-silica Composite: kinetics, Isotherms and thermodynamics studies," *Advanced Materials Letters*, vol. 7, no. 8, pp. 673–678, 2016.

[52] P. M. Thabede, N. D. Shooto, T. Xaba, and E. B. Naidoo, "Magnetite functionalized Nigella sativa seeds for the uptake of chromium(VI) and lead(II) ions from synthetic wastewater," *Adsorption Science & Technology*, vol. 2021, pp. 1–15, 2021.

[53] W. Zhang, Y. An, S. Li et al., "Enhanced heavy metal removal from an aqueous environment using an eco- friendly and sustainable adsorbent," *Scientific Reports*, vol. 10, no. 1, p. 16453, 2020.

[54] A. N. Baghani, A. H. Mahvi, M. Gholami, N. Rastkari, and M. Delikhoon, "One-Pot synthesis, characterization and adsorption studies of amine-functionalized magnetite nanoparticles for removal of Cr (VI) and Ni (II) ions from aqueous solution: kinetic, isotherm and thermodynamic studies," *Journal of Environmental Health Science & Engineering*, vol. 14, p. 11, 2016.

[55] F. Tsegaye, A. M. Taddesse, E. Teju, and M. Aschalew, *Bulletin of the Chemical Society of Ethiopia*, vol. 34, no. 1, pp. 105–121, 2020.

[56] F. L. Rivera, F. J. Palomares, P. Herrasti, and E. Mazario, "Improvement in heavy metal removal from wastewater using an external magnetic inductor," *Nanomaterials*, vol. 9, no. 11, p. 1508, 2019, [CrossRef]].

[57] Y. Bagbi, A. Sarswat, D. Mohan, A. Pandey, and P. R. Solanki, "SciENtific REPOrTS, Lead and chromium adsorption from water using L-cysteine functionalized magnetite (Fe3O4)," *Nano*, vol. 7, no. 1, article 7672.

[58] S. Tao, C. Wang, W. Ma, S. Wu, and C. Meng, "Designed multifunctionalized magnetic mesoporous microsphere for sequential sorption of organic and inorganic pollutants," *Microporous and Mesoporous Materials*, vol. 147, no. 1, pp. 295–301, 2012.

[59] M. Zaki, A. Maulana, F. Tirtayani, P. N. Alam, and H. Husin, "Mercury removal in wastewater by iron oxide nanoparticles," *Journal of Physics: Conference Series*, vol. 687, article 012050, 2016.

[60] H. Parham, B. Zargar, and R. Shiralipour, "Fast and efficient removal of mercury from water samples using magnetic iron oxide nanoparticles modified with 2-mercaptobenzothiazole," *Journal of Hazardous Materials*, vol. 205-206, pp. 94–100, 2012.

[61] H. Kumar, S. K. Sinha, V. V. Goud, and S. Das, "Removal of Cr(VI) by magnetic iron oxide nanoparticles synthesized from extracellular polymeric substances of chromium resistant acid-tolerant bacterium Lysinibacillus sphaericus RTA-01," *Journal of Environmental Health Science and Engineering*, vol. 17, no. 2, pp. 1001–1016, 2019.

[62] M. Agarwal, P. Dey, S. Upadhayaya, and R. Dohare, "Adsorption efficiency of magnetite nanoparticles for chromium(VI) removal from water," *Journal of the Indian Chemical Society*, vol. 93, pp. 199–209, 2016.

[63] N. Saber, M. Duaa, and M. Naji, "Statistical analysis of the removal of Chromium(VI)by Iron Oxide Nanoparticle (Fe3O4)," *Journal of Engineering*, vol. 24, 2018.

[64] S. Liang, S. Shi, H. Zhang et al., "One-pot solvothermal synthesis of magnetic biochar from waste biomass: Formation mechanism and efficient adsorption of Cr(VI) in an aqueous solution," *Science of the Total Environment*, vol. 695, article 133886, 2019.

[65] J. Zhang, S. Lin, M. Han, S. Qing, L. Xia, and Z. Hui, "Adsorption properties of magnetic magnetite nanoparticle for coexistent Cr(VI) and Cu(II) in mixed solution," *Watermark*, vol. 12, no. 2, p. 446, 2020.